MOF-Derived Multi-heterostructured Composites for Enhanced Photocatalytic Hydrogen Evolution

Deciphering the Roles of Different Components

Hussain, Mian Zahid; Yang, Zhuxian; Van Der Linden, Bart; Heinz, Werner R.; Bahri, Mounib; Ersen, Ovidiu; Jia, Quanli; Fischer, Roland A.; Zhu, Yanqiu; Xia, Yongde

DOI
10.1021/acs.energyfuels.2c02319

Publication date
2022

Document Version
Final published version

Published in
Energy and Fuels

energy&fuels

pubs.acs.org/EF

Article

MOF-Derived Multi-heterostructured Composites for Enhanced Photocatalytic Hydrogen Evolution: Deciphering the Roles of Different Components

Mian Zahid Hussain,* Zhuxian Yang, Bart van der Linden, Werner R. Heinz, Mounib Bahri, Ovidiu Ersen, Quanli Jia, Roland A. Fischer, Yanqiu Zhu, and Yongde Xia*

Cite This: https://doi.org/10.1021/acs.energyfuels.2c02319

Read Online

ACCESS | Metrics & More | Article Recommendations | Supporting Information

ABSTRACT: Bimetal-organic-framework (Bi-MOF) NH_2-MIL-125(Ti/Cu)-derived nanocomposites are systematically investigated to elucidate the role of individual species TiO_2, Cu_xO and the porous carbon matrix in photocatalytic activity. Among the studied samples, the $TiO_2/Cu_xO/C$ nanocomposite derived from heat processing NH_2-MIL-125(Ti/Cu) under Ar/H_2O vapor demonstrates the highest photocatalytic H_2 evolution performance due to the formation of a phasejunction between the well-crystallized anatase/rutile TiO_2 polymorph, the optimized and codoped nitrogen/carbon in the composites, the formation of p−n heterojunctions between the TiO_2 and Cu_xO nanoparticles, as well as their uniform distribution in a hydrophilic porous carbon matrix decorated with N and carboxylic functional groups. These parameters enable the in situ-formed multi-heterostructures in these nanocomposites to not only possess relatively narrower energy band gaps and improved spatial charge separation due to the formed type-II staggered p−n heterojunctions but also offer multiple pathways for charge diffusion, resulting in lower charge-transfer resistance, suppressed bulk charge recombination, and consequently, much improved visible-light absorption. Therefore, the Bi-MOF NH_2-MIL-125(Ti/Cu)-derived $TiO_2/Cu_xO/C$ nanocomposite provides easily accessible active sites with an excellent photocatalytic H_2 evolution activity of 3147 μmol g_{cat}^{-1} h^{-1}, 99 times higher than that of bare TiO_2. This work provides a simple one-step approach to producing tunable novel nanocomposites for efficient photocatalytic H_2 evolution without using expensive noble metals as cocatalysts.

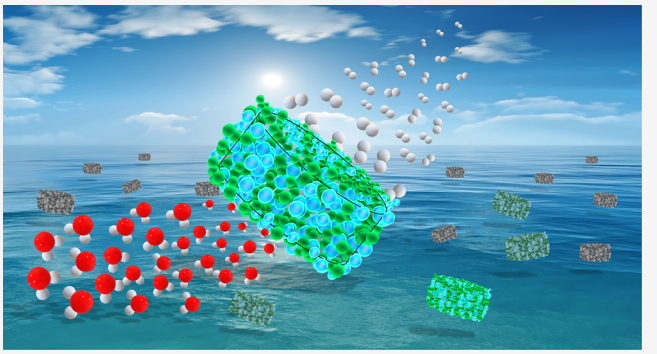

INTRODUCTION

Renewable energy sources are regarded as the most plausible alternatives to fossil fuels and nuclear energy to deal with the global challenges of climate change and environmental pollution.[1] The generation of green hydrogen (H_2) from photocatalytic water splitting is one of the viable solutions to produce an environmentally sustainable and cost-effective clean fuel to be directly used in automobiles, domestic heating, fuel cells, and industrial applications.[2,3] Currently, H_2 is largely produced by economically expensive and environmentally unsustainable processes such as methane steam reforming.[4] Since Fujishima demonstrated in 1972 that the solar-light-driven H_2 evolution imitates the photosynthesis process, much effort has been dedicated to searching for chemically stable and highly efficient photocatalysts.[2,5]

Most of the semiconducting photocatalysts possess wide energy band gaps (EBGs), which leads to poor photocatalytic performance due to the limited absorption of light and the higher recombination of photogenerated charge. Various strategies, such as defect generation, and doping of cationic (metal atoms) and/or anionic (C, N, S, P) species into the photocatalyst, which narrows down the EBGs, have been adapted to improve the photocatalytic performance.[6−8] Alternatively, photoactive multimetal compounds can be combined to generate heterostructures as well as metal and/or nonmetal composites that can synergistically improve the photocatalytic activities.[9−11] An ideal photocatalyst for hydrogen evolution reaction (HER) should absorb maximum light in the UV−visible and IR regions of the electromagnetic spectrum and produce the corresponding number of photogenerated charge carriers to the redox reaction with minimum charge recombination.[9,10] In addition, it should exhibit long-term chemical and physical stability for constant H_2 evolution.[9]

Received: July 11, 2022
Revised: August 17, 2022
Published: September 1, 2022

Since the early demonstrations of photoelectrochemical performance of TiO_2-based materials, TiO_2 has been one of the most promising semiconducting materials due to its photocatalytically suitable optoelectronic properties.[2,9] Although the wider EBG (3.2 eV) and the limited absorption of incident light in the UV region restrict TiO_2 from being directly employed in photocatalytic reactions,[6] the EBG of TiO_2 can be easily tuned by controlled doping of anionic and/or cationic species for better light absorption in the visible region of the light spectrum. However, charge recombination in such single metal oxide photocatalysts is still a challenge since photocharge generation/recombination takes place at the time scale of femtoseconds to picoseconds, whereas the catalytic reactions usually occur at the time scale of microseconds to milliseconds.[9,12] Therefore, to develop a successful photocatalyst, it is necessary to prolong the lifetime of the photogenerated charges, which can be realized by spatially separating the photogenerated charge carriers to maximize the interaction between the catalytically reactive species and photogenerated electrons/holes at the respective active sites for enhanced quantum yield. Together with the optoelectronic properties, the chemical composition and the morphology of the photocatalyst play important roles in determining the lifetime and diffusion lengths of the photogenerated charge carriers.[9] The spatial separation of charge carriers, their diffusion path (length), and the catalytic activity in the semiconducting photocatalysts can be modified through various methods, including rational design of structures, atomically precise control of chemical compositions, optimized morphologies, and precise construction of interfaces of (multi)metal compound heterostructures.[6] Many approaches to synthesizing such photocatalytically efficient systems have been reported; however, these approaches generally require multistep, complex, and relatively expensive processes, which make them practically unaffordable.[6,7]

Metal−organic frameworks (MOFs) are excellent materials due to their structural, morphological, and textural properties, offering chemically active inorganic and organic moieties. They possess extraordinarily high surface areas, modifiable textural properties, and accessible photocatalytic active sites.[13,14] Despite these unique properties, the relatively poor semiconducting properties restrict the pristine MOFs from being directly employed as photocatalysts.[15] However, MOFs are excellent sacrificial templates or precursors to derive an unlimited variety of photocatalytically efficient nanocomposites, which offer great flexibility to rationally design and modify the morphology, dimensionality, chemical composition, textural, optoelectronic, and semiconducting properties.[16−21] All of these properties play very important roles in determining the photocatalytic activity of a catalyst. In this context, some fundamentally important questions need to be addressed. For instance, where does the photocatalytic activity in such chemically complex, MOF-derived nanocomposites originate from? What role do the derived metal oxides and carbon species play in the absorption of incident light and photocatalytic H_2 evolution? Based on some in situ characterizations and in-depth analyses of nanocomposites derived from NH_2-MIL-125(Ti/Cu), this work offers useful insights into optical and physicochemical properties of the derived composites to decipher the role of metal oxides (TiO_2, Cu_xO) and porous carbon in photocatalytic H_2 evolution.

EXPERIMENTAL SECTION

Synthesis of NH_2-MIL-125(Ti). The NH_2-MIL-125(Ti) was synthesized by following a previously reported method with some modifications for scaling up.[22,23] In a typical synthesis, 30 mmol of 2-aminoterephthalic acid was dissolved in 75 mL of dimethylformamide (DMF) and methanol (MeOH) (1:1) in a screw jar under stirring (800 rpm) for 0.5 h. Once the organic linker was fully dissolved, 10 mmol of titanium butoxide [$Ti(OBu)_4$] was added slowly followed by placing it at 130 °C in an oil bath. After 40 h, the NH_2-MIL-125(Ti) yellow precipitate was collected, centrifuged (7800 rpm for 15 min), and washed several times with methanol for the removal of unreacted species and complete solvent exchange. The synthesized NH_2-MIL-125(Ti) was dried in a vacuum oven at 80 °C overnight.

Synthesis of NH_2-MIL-125(Ti/Cu). As a second metal, Cu was loaded into NH_2-MIL-125(Ti) via a postsynthesis modification method[24,25] rather than the conventional one-pot synthesis.[26] Typically, 2 g of dried NH_2-MIL-125(Ti) was dispersed in 200 mL of MeOH and DMF and ultrasonicated for 3 h. A $Cu(NO_3)_2{\cdot}3H_2O$ (0.86 g) solution in MeOH (20 mL) was poured into the NH_2-MIL-125(Ti) dispersion followed by heating at 110 °C for 12 h. The dark-green powder of Cu-loaded NH_2-MIL-125(Ti/Cu) was centrifuged and washed multiple times in MeOH for complete removal of unreacted Cu species followed by drying in a vacuum oven at 80 °C.

Synthesis of the Derived Nanocomposites. As-prepared NH_2-MIL-125(Ti) and NH_2-MIL-125(Ti/Cu) were heat-treated in a flow-through quartz tube furnace for 2 h with a ramp rate of 5 °C min^{-1} at 700 °C under air to derive TiO_2 and TiO_2/CuO, respectively, and under argon saturated with water vapor (Ar/H_2O) to obtain TiO_2/C and TiO_2/Cu_xO/C nanocomposites, respectively. When the tube furnace reached the target temperature of 700 °C, the water vapor (as a mild oxidizing agent) was carried by argon gas passing through a water buffer bottle at room temperature with the flow rate of 50 mL·min^{-1} during the dwell time only. The sample prepared from NH_2-MIL-125(Ti/Cu) under Ar/H_2O was named $TiO_2/Cu_xO/C_{2h}$. For simplicity, this sample is denoted as TiO_2/Cu_xO/C in the manuscript. Two more samples were prepared under an identical temperature and gas atmosphere but with different dwell times of 0.5 and 4 h to study the effect of the pyrolysis time on the derived nanocomposites. The resulting products were labeled as $TiO_2/Cu_xO/C_{0.5h}$ and $TiO_2/Cu_xO/C_{4h}$, respectively.

Material Characterizations and Photocatalytic HER Measurements. Powder X-ray diffraction (PXRD) patterns of the sacrificial templates MOFs and the derived nanocomposites were recorded by *Bragg-Brentano* geometry in a *PANalytical* Empyrean diffractometer (Cu Kα λ_1 = 1.5406 Å, λ_2 = 1.5444 Å, I_2/I_1 = 0.5, V = 45 kV, and I = 40 mA) equipped with a *PANalytical* PIXcel 1D detector. The morphologies and surface texture of the samples were recorded by an xT Nova Nanolab 600 FIB coupled with in situ scanning electron microscopy (SEM) all in one unit. High-resolution images and elemental maps of the samples were recorded with transmission electron microscopy (TEM) equipped with energy-dispersive X-ray spectroscopy (EDX) (JEM 2100 LeB6 200 kV). For in situ scanning transmission electron microscopy (STEM), a Jeol 2100 F FEG (200 kV) with a spherical aberration corrector, operating in bright-field (BF)-STEM or high-angle annular dark (HAADF)-STEM modes with a resolution of 0.11 nm, was used. The Mettler Toledo thermogravimetric analysis/differential scanning calorimetry (TGA/DSC) 3 connected to mass spectrometry (MS) was employed for thermogravimetric analysis of activated MOFs and their derived composites in synthetic air and under Ar. To record the Raman spectra of the samples, Renishaw inVia Reflex Raman System RL532C, Class 3B (50−3000 cm^{-1}), was used. The X-ray photoelectron spectroscopy (XPS) data was collected by employing the Kratos Axis Ultra DLD spectrometer with a monochromated Al Kα X-ray source operating at 168 W (12 mA × 14 kV). The collected XPS data from all of the samples were analyzed using CasaXPS software (v2.3.23). XPS depth profiling of NH_2-MIL-125(Ti/Cu) was carried out to confirm the uniform atomic distribution of each element including loaded Cu. The measurement was performed using

https://doi.org/10.1021/acs.energyfuels.2c02319
Energy Fuels XXXX, XXX, XXX−XXX

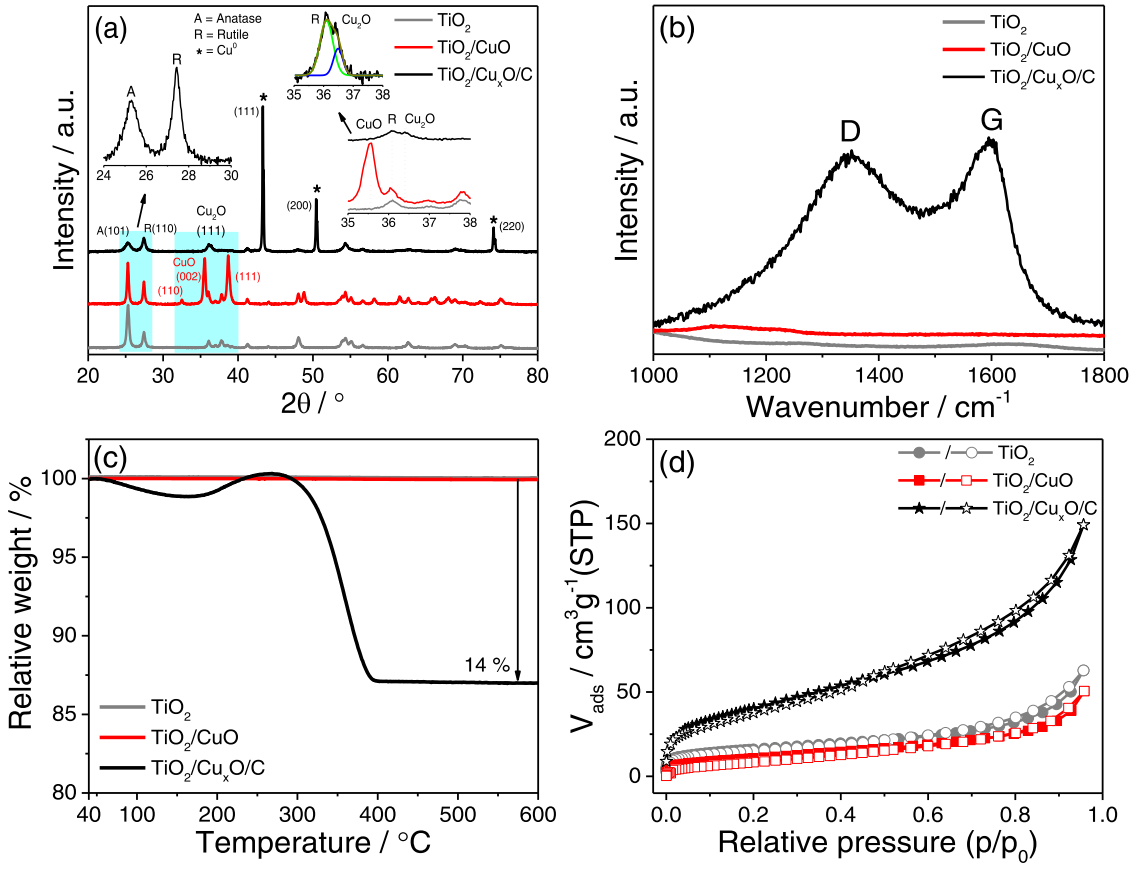

Figure 1. (a) PXRD patterns, (b) Raman spectra, (c) TGA profiles in air, and (d) N_2 sorption isotherms of NH_2-MIL-125(Ti)- and NH_2-MIL-125(Ti/Cu)-derived TiO_2 (gray), TiO_2/CuO (red), and TiO_2/Cu_xO/C (black) nanocomposites. The solid and empty symbols in (d) represent the adsorption and desorption branches of N_2 isotherms, respectively.

a 110 μm-diameter spot after etching over an area of 2 × 2 mm^2 by Ar (1 × 10^{-6} Torr) at 4 kV. The UV−vis absorption spectra of the samples were measured using a ThermoScientific Evolution 200 spectrophotometer. The collected XPS spectra were calibrated with respect to adventitious carbon peaks at 284.8 eV (C 1s). The Brunauer−Emmett−Teller (BET) surface areas and the distribution of pore sizes of the samples were measured by the 3Flex instrument (Micromeritics). The samples were degassed for 3 h at 180 °C under a vacuum. The pore size was calculated by nonlocal density functional theory (NLDFT) applying the Tarazona model (cylindrical pores) for nanoporous materials. The electrochemical impedance spectra (EIS) and transient photocurrent density at room temperature were recorded by the CHI660E electrochemical workstation (a three-electrode setup). A carbon rod and Ag/AgCl were used as counter and reference electrodes, respectively. A glassy carbon (GC) (2.8 cm^2, finely polished) electrode was used as a working electrode. To prepare the ink for the working electrode, 1 mg of photocatalyst was dispersed in 500 μL of ethanol/water (1:4 v/v) solution and 5 μL of Nafion solution (5 wt %) by ultrasonication. A 0.1 M $HClO_4$ solution was used as an electrolyte for all EIS measurements. For transient photocurrent density, the linear sweep voltammetry (LSV) was recorded at a constant potential of −0.4 V (in 0.5 M H_2SO_4) under a simulated light source (Newport, 400 W Xe/Hg lamp). The electron paramagnetic resonance (EPR) spectrum of a selected sample was recorded by an X-band CWEPR Bruker EMX spectrometer (Oriel Instruments, 600 W xenon lamp with an IR water filter) at 100 kHz field modulation.

Photocatalytic H_2 evolution reaction (HER) tests of the derived composites were performed in a Pyrex-glass reactor (volume of 42.1 mL including a headspace of 17.1 mL for collection of generated gases) coupled with a CP 9001 gas chromatograph. All HER tests were performed under the isothermal condition (at 30 °C) using a 500 W Xe/Hg lamp (66 983, Newport) with a 285 nm cutoff optical filter. For each measurement, 10 mg of the photocatalyst was dispersed in a solution of deionized water (17.5 mL), and methanol (7.5 mL) was used as the sacrificial agent for hole compensation and put in the reactor under magnetic stirring and purged for 30 min under a constant Ar flow of 30 mL min^{-1} to ensure complete deoxygenation of the system. The apparent quantum yield (AQY %) of the measured samples was calculated by the following equation[27]

$$AQY_{\lambda} = \frac{2 \times \text{Number of evolved } H_2 \text{ molecules}}{\text{Total number of incident photons}} \times 100\% \quad (1)$$

RESULTS AND DISCUSSION

Chemical Composition, Crystallinity, and Textural Properties. PXRD patterns (Figure S1a) confirm the synthesis of the precursor MOF NH_2-MIL-125(Ti) and the loading of Cu^{2+} into NH_2-MIL-125(Ti/Cu). After the coordination of Cu^{2+} species with the amino functional group (NH_2) attached to the organic linker, no additional peaks of Cu were observed. The N_2 sorption of activated precursors NH_2-MIL-125(Ti) and NH_2-MIL-125(Ti/Cu) exhibits typical type I isotherms (Figure S1b), confirming the microporous nature of these MOF materials with well-defined micropores (Figure S1c). It is inevitable that NH_2-MIL-125(Ti/Cu) shows a slight decrease in the surface area due to the loading of Cu species. Table S1 summarizes their BET surface area, pore diameter, and pore volume. To further confirm the homogeneous distribution of Cu atoms into NH_2-MIL-125(Ti), spherical aberration-corrected STEM-HAADF

https://doi.org/10.1021/acs.energyfuels.2c02319
Energy Fuels XXXX, XXX, XXX−XXX

Table 1. Textural Properties, Crystallinity, Energy Band Gap, and Photocatalytic HER Activity of the Derived Nanocomposites

Sample	Textural properties		A (101)/R (110) phase percentage (%)	EBG (eV)	H_2 evolution (μmol g_{cat}^{-1} h^{-1})	AQY at 435 nm (%)
	Surface area (m^2 g^{-1})	Total pore volume (cm^3 g^{-1})				
TiO_2	56.4	0.094	73.5/26.5	2.96	31.8	0.08
TiO_2/CuO	37.2	0.075	63/37	2.64	2340	5.52
TiO_2/C	378	0.33	44/56	2.91	426	2.45
$TiO_2/Cu_xO/C_{0.5h}$	250	0.365	72.5/27.5	2.33	1227	2.90
$TiO_2/Cu_xO/C_{2h}$	144	0.224	51/49	2.45	3147	7.66
$TiO_2/Cu_xO/C_{4h}$	155	0.245	40/60	2.38	2338	5.52

images (Figure S2) of NH_2-MIL-125(Ti/Cu) (before and after Cu loading) were recorded. In Figure S2b, Cu species loaded into NH_2-MIL-125(Ti) can be observed as white dots. The high-resolution STEM (Figure S2c) image of NH_2-MIL-125(Ti/Cu) and the selected area electron diffraction pattern (Figure S2d) confirm the nonagglomerated and uniformly distributed Cu species. Moreover, the XPS depth profiling of the precursor NH_2-MIL-125(Ti/Cu) was carried out to quantify the uniform distribution of the elemental species in crystals, including Ti, Cu, N, O, and C. The depth profiling (etched depth up to 240 nm) (Figure S3) confirms that the averaged values of atomic concentrations (at. conc. %) of Ti 2p, Cu 2p, C 1s, O 1s, and N 1s were 10.6, 4, 61, 19, and 5.4%, respectively.[23,24] In addition, a detailed TGA-MS analysis of thermal decomposition of the precursor NH_2-MIL-125(Ti/Cu) under air and under an inert gas atmosphere is provided in Figure S4.[24]

Depending upon the gaseous atmosphere during the heating process, MOFs transform into metal oxides or metal oxide/carbon composites at higher temperatures.[16,28,29] Figure 1a shows the PXRD patterns of NH_2-MIL-125(Ti) and NH_2-MIL-125(Ti/Cu)-derived TiO_2, TiO_2/CuO under air and $TiO_2/Cu_xO/C$ under Ar/H_2O at 700 °C. In all three derived samples, the signature XRD peak of TiO_2 appeared at 25.3° for the anatase (101) and at 27.4° for the rutile (110) phase. However, compared to the samples derived under Ar/H_2O, the anatase phase is dominant in samples derived in the air. The anatase-to-rutile-phase ratio (A/R %) values of the TiO_2 polymorph are determined to be 73.5/26.5, 63/37, and 51/49 for samples TiO_2, TiO_2/CuO, and $TiO_2/Cu_xO/C$, respectively. This is because the thermal decomposition of the precursor NH_2-MIL-125(Ti/Cu) under an inert atmosphere proceeds slowly compared to the thermal decomposition in air (Figure S4a,b). Moreover, the in situ formation of carbon from the organic linker (NH_2-BDC) of MOFs under Ar/H_2O also influences the localized chemical environment, resulting in the relatively higher growth of the rutile phase of TiO_2 compared to the anatase TiO_2 phase. The sample $TiO_2/Cu_xO/C$ derived under Ar/H_2O for 2 h of dwell time exhibits an almost 1:1 A/R phase ratio of TiO_2 polymorphs, which is ideal for the formation of a phasejunction.[10] The particle sizes of the A/R TiO_2 polymorph (by the Scherrer equation) were calculated to be 19.3/19.5, 27.3/24.9, and 8.3/13.9 nm for the samples TiO_2, TiO_2/CuO, and $TiO_2/Cu_xO/C$, respectively. The formation of relatively smaller TiO_2 nanoparticles under an Ar/H_2O atmosphere is directly influenced by the presence of carbon (from the organic linker), which prevents the smaller nanoparticles from sintering/agglomerating, resulting in the immobilization and uniform distribution of TiO_2 species embedded in the porous carbon matrix.[22] These smaller particle sizes are likely to offer increased photocatalytic active sites.

To investigate the effect of pyrolysis time on the crystallinity and phase ratios of TiO_2 and Cu_xO species in the derived composites, two more samples, $TiO_2/Cu_xO/C_{0.5h}$ and $TiO_2/Cu_xO/C_{4h}$, at different dwell times of 0.5 and 4 h, respectively, were prepared. PXRD results of those samples (Figure S5) suggest that in the sample $TiO_2/Cu_xO/C_{0.5h}$, TiO_2 remains poorly crystalline with a dominant anatase phase (A/R ratio of 72.5/27.5), and the Cu_xO species (highlighted in the inset) exhibit a broader peak with a lower intensity, indicating that they are mainly amorphous. However, in the sample $TiO_2/Cu_xO/C_{4h}$, TiO_2 shows a significant improvement in crystallinity, with the rutile phase outgrowing the anatase phase (A/R ratio of 40/60) due to the longer dwell time at the target temperature. In addition, Cu_xO also exhibits relatively better crystallinity in this sample. The phase ratios and particle sizes of TiO_2 nanoparticles in the derived composites are summarized in Table 1. Obviously, in NH_2-MIL-125(Ti/Cu)-derived multi-heterostructured $TiO_2/Cu_xO/C$ nanocomposites, a heating time of 2 h at 700 °C is the optimum condition to form a good crystalline phasejunction between the TiO_2 polymorph with an A/R ratio of 1:1, which is consistent with previous observations.[22,24]

In the composite derived from NH_2-MIL-125(Ti/Cu) under air, Cu is fully oxidized to CuO at 700 °C, which is confirmed by the signature PXRD peak, appearing at 2θ of 35.5°. However, under a water vapor atmosphere, the Cu species are partially oxidized to Cu_2O accompanied by a small amount of CuO as well as a significant amount of Cu^0.[17,24] This is due to the fact that the reduction potential of Cu^{2+} is above −0.27 V, which results in the Cu^{2+} species in the MOF precursor transforming into pure Cu^0 nanoparticles upon pyrolysis under inert conditions.[17] In Ar/H_2O, a mildly oxidizing atmosphere is established by introducing regulated water vapor at the target temperature of 700 °C, which partially oxidizes the Cu species into Cu_2O. The signature PXRD peak for Cu_2O (highlighted in the inset) appeared at 2θ of 36.4°, and characteristic PXRD peaks of Cu^0 are observed at 2θ of 43.3, 50.4, and 74.1°. It can be anticipated that the optimized anatase/rutile ratio of TiO_2 benefits the formation of a phasejunction between TiO_2 and p−n heterojunctions between TiO_2 and Cu_xO during the pyrolysis of NH_2-MIL-125(Ti/Cu) at 700 °C.

As discussed above, heat treatment of MOFs and Bi-MOFs in air results in metal oxides, while metal oxide/carbon composites are obtained under Ar/H_2O. To investigate the nature of carbon, Raman spectra of these derived samples were recorded. As expected, no characteristic Raman peaks of carbon are observed in TiO_2 and TiO_2/CuO derived under air; however, signature carbon peaks of D and G bands appeared at

https://doi.org/10.1021/acs.energyfuels.2c02319
Energy Fuels XXXX, XXX, XXX−XXX

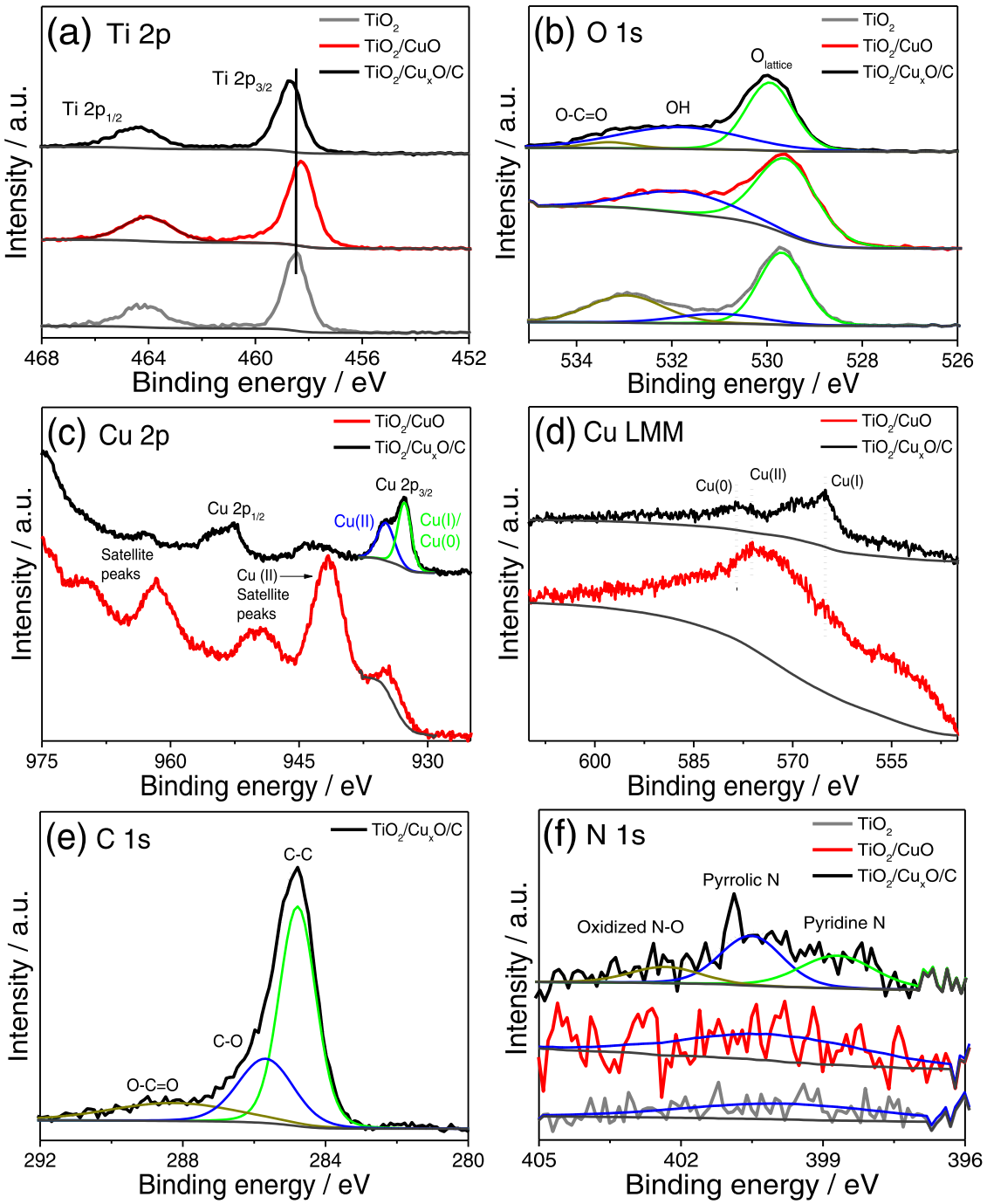

Figure 2. XPS spectra of elements (a) Ti 2p, (b) O 1s, (c) Cu 2p, (d) Cu LMM, (e) C 1s, and (f) N 1s of the derived TiO_2, TiO_2/CuO, and $TiO_2/Cu_xO/C$.

around 1349 and 1595 cm^{-1} in $TiO_2/Cu_xO/C$ (Figure 1b), which correspond to the defects/disorders in carbon and the graphitic/nanocrystalline carbon, respectively.[30,31] The I_D/I_G ratio indicates the formation of various defects in carbon. In the sample $TiO_2/Cu_xO/C$, the I_D/I_G ratio is calculated to be 0.92, which signifies the formation of defects and the presence of nitrogen- and oxygen-related surface species on the carbon matrix.[24] The TGA profiles (Figure 1c) of the derived composites in the air atmosphere also confirmed that no carbon is present in the derived TiO_2 and TiO_2/CuO samples. However, the sample $TiO_2/Cu_xO/C$ obtained under Ar/H_2O exhibits a 14% weight loss between 300 and 400 °C, indicating the presence of a significant amount of carbon, from the organic linker.[32,33]

The N_2 sorption of derived samples TiO_2, TiO_2/CuO, and $TiO_2/Cu_xO/C$ exhibits type IV isotherms with a small hysteresis above the relative pressure (p/p_0) of 0.4 (Figure 1d), indicating the emergence of mesopores due to the collapse of the MOF framework. The specific surface areas of the derived samples TiO_2, TiO_2/CuO, and $TiO_2/Cu_xO/C$ are 56, 37, and 144 $m^2\ g^{-1}$, respectively. The relatively low surface areas in the derived metal oxides are because all of the carbon from the organic linker (NH_2-BDC) is oxidized in the form of NO_x, CO, and CO_2 (confirmed by TGA-MS). However, the

https://doi.org/10.1021/acs.energyfuels.2c02319
Energy Fuels XXXX, XXX, XXX−XXX

$TiO_2/Cu_xO/C$ composite, derived under the Ar/H_2O atmosphere, exhibits a moderate BET surface area due to the presence of 14 wt % porous carbon, as confirmed by TGA under air in Figure 1c. Generally, in MOF-derived composites, a higher amount of porous carbon provides a higher BET surface area, which leads to a better distribution of metal oxide species throughout the carbon matrix. Consequently, it prevents the agglomeration of metal oxides and provides additional photocatalytic active sites. The textural properties of NH_2-MIL-125(Ti/Cu)-derived composites under Ar/H_2O at 700 °C for variable dwell times were also investigated. The N_2 sorption isotherms of $TiO_2/Cu_xO/C_{0.5h}$ and $TiO_2/Cu_xO/C_{4h}$ are shown in Figure S6; the surface areas and pore volumes of the derived composites are summarized in Table 1. The sample $TiO_2/Cu_xO/C_{0.5h}$ exhibits a relatively higher surface area of 250 $m^2\ g^{-1}$ compared to the samples $TiO_2/Cu_xO/C_{2h}$ (144 $m^2\ g^{-1}$) and $TiO_2/Cu_xO/C_{4h}$ (155 $m^2\ g^{-1}$), which may be due to the fact that the sample $TiO_2/Cu_xO/C_{0.5h}$ is prepared at a shorter dwell time (0.5 h), and there is a relatively higher amount of porous carbon present in this sample. On the contrary, in the sample prepared for a longer dwell time (4 h), most of the carbon is partially oxidized into CO/CO_2, leaving only a small amount present in the sample. Despite the lower C content, the sample $TiO_2/Cu_xO/C_{4h}$ exhibits a relatively high surface area because the controlled and partial oxidization of carbon prevents the TiO_2 and Cu_xO nanoparticles from agglomeration and retains the inherited morphology, which results in a slightly higher N_2 sorption. TGA combined with MS spectra of the sample $TiO_2/Cu_xO/C_{4h}$ (Figure S7a,b) confirms the release of CO_2 along with H_2O and NO. Interestingly, the weight loss between 300 and 500 °C due to the oxidization of carbon species (releasing in the form of CO_2) coincides with the weight gain due to the oxidization of Cu^0 into CuO.

The X-ray photoelectron spectroscopy (XPS) peaks of Ti $2p_{3/2}$ (Figure 2a) in the derived samples TiO_2, TiO_2/CuO, and $TiO_2/Cu_xO/C$ appear at 458.5, 458.3, and 458.7 eV, respectively, which confirm that Ti^{4+} oxidation state exists in all three samples. A small shift of 0.2 eV in the core level (Ti $2p_{3/2}$) in samples TiO_2/CuO and $TiO_2/Cu_xO/C$ compared to the bare TiO_2 indicates the band-bending at the interfacial surface due to the formation of a p−n heterojunction between TiO_2 and CuO.[34] Additionally, the presence of doped N and C species in the sample $TiO_2/Cu_xO/C$ also modifies the local electronic and chemical environment of Ti atoms due to the formation of Ti−N and Ti−C bonds and oxygen-related defects present in the TiO_2 crystal lattice.[22,24,35] This is further confirmed by the C 1s and N 1s spectra. The deconvoluted O 1s peaks (Figure 2b) of the derived sample TiO_2 are observed at 529.7, 531.1, and 533.0 eV, which can be assigned to $O_{lattice}$ (Ti−O and Cu−O), surface-absorbed OH, and C═O groups, respectively. A small shift of 0.2 eV in the $O_{lattice}$ peak in samples TiO_2/CuO and $TiO_2/Cu_xO/C$ (consistent with Ti $2p_{3/2}$) confirms the formation of p−n heterojunction, as well as the presence of defects and vacancies due to the oxygen vacancies and doped N/C species.[6−8] The peak observed at 533.4 eV in the sample $TiO_2/Cu_xO/C$ composite can be ascribed to the carboxylic (O═C−O) groups functionalized on the surface of the porous carbon matrix.[36]

In $TiO_2/Cu_xO/C$, two main deconvoluted peaks of the core-level Cu $2p_{3/2}$ appearing at 932.9 and 934.9 eV (Figure 2c) are assigned to the Cu(I)/Cu(0) and Cu(II) oxidation states, respectively. Usually, during the pyrolysis of Cu-MOFs under an inert atmosphere, Cu is reduced to Cu^0 particles.[17,28] However, the oxidation state of Cu species can be controlled by optimizing the pyrolysis conditions including the gas atmosphere, the pyrolysis temperature, and the dwell time. In the sample TiO_2/CuO, the Cu $2p_{3/2}$ peak observed at 934.4 eV (and a strong satellite peak at 941.6 eV) confirms the Cu(II) oxidation state.[34,37] The Cu species are fully oxidized to CuO during the heating of NH_2-MIL-125(Ti/Cu) up to 700 °C in air; however, under Ar/H_2O, the Cu species are partially oxidized to Cu_2O/CuO (with a dominant Cu(I) state) due to the limited exposure to oxygen. Therefore, a significant amount of Cu is found in the Cu(0) state in $TiO_2/Cu_xO/C$. The shift in binding energies (B.E.) and the intensities of the Cu $2p_{3/2}$ in these two samples (obtained under Ar/H_2O and under air, respectively) clearly indicates the critical role of the gaseous atmosphere in MOF derivation,[24] as also confirmed by PXRD patterns in Figure 1a. The high-resolution XPS spectra of Cu LMM can better distinguish the oxidation states of the Cu species. As shown in Figure 2d, the high-resolution XPS Cu LMM peaks observed at 565.1, 576.3, and 578.6 can be assigned to Cu(I), Cu(II), and Cu(0), respectively.[38,39] These observations confirm that Cu(II) is the primary oxidation state in the sample TiO_2/CuO obtained under air, whereas Cu species predominantly form Cu(I) and Cu(0) oxidation states in the sample $TiO_2/Cu_xO/C$ under Ar/H_2O.

The C 1s XPS peaks (Figure 2e) appearing at 284.8, 285.7, and 288.5 eV in $TiO_2/Cu_xO/C$ are assigned to the sp^2 bonded C═C, sp^3 bonded C−C, and surface-functionalized carboxylate (O−C═O) groups, respectively.[35,40] These (OH/COOH) functional groups present on the porous carbon matrix in samples derived under an Ar/H_2O atmosphere enhance the hydrophilic behavior of the sample and improve the water−catalyst interaction, resulting in better photocatalytic activity.[24,36] The N 1s XPS spectrum (Figure 2f) of $TiO_2/Cu_xO/C$ is deconvoluted into three peaks observed at B.E. values of 398.7, 400.5, and 402.4 eV, representing pyridinic N, pyrrolic N species, and oxidized N species (N−O), respectively.[33,41,42] This observation shows good consistency with recently published works.[22,24] During the pyrolysis of the precursor NH_2-MIL-125(Ti/Cu) under Ar/H_2O, the N atoms from the cleaved-off organic linker (2-aminoterephthalic acid) replace O atoms, resulting in in situ interstitial N atoms doping into TiO_2. It also creates defects and oxygen vacancies in the TiO_2 crystal lattice. Due to the oxygen-saturated atmosphere in the Ar/H_2O atmosphere, oxygen-rich N−O-like interstitial/intraband states are formed.[22,43] In the sample $TiO_2/Cu_xO/C$, the deconvoluted N 1s peak observed at 402.4 eV can be assigned to these oxygen-rich N−O-like intraband/interstitial states formed above the valence band (V.B.) of TiO_2. This observation is further supported by XPS valence band edge spectra as well as UV−vis absorption spectroscopy. In samples TiO_2 and TiO_2/CuO prepared in air, a broad, low-intensity N 1s peak is observed at around 400 eV, indicating the presence of doped interstitial N sites into TiO_2 (N−Ti−O).[8,43] However, in these samples, no additional peaks for surface-functionalized N species are observed. The low intensity of the N 1s peaks is due to the fact that on heat processing of MOF precursors at high temperatures, most of the N species (from the organic linker, 2-aminoterephthalic acid) is oxidized and released in the form of NO_x. Only a trace amount of N doped into TiO_2 is left behind. However, when the sample $TiO_2/Cu_2O/C$ was prepared under Ar/H_2O (water steam), the organic linker only

https://doi.org/10.1021/acs.energyfuels.2c02319
Energy Fuels XXXX, XXX, XXX−XXX

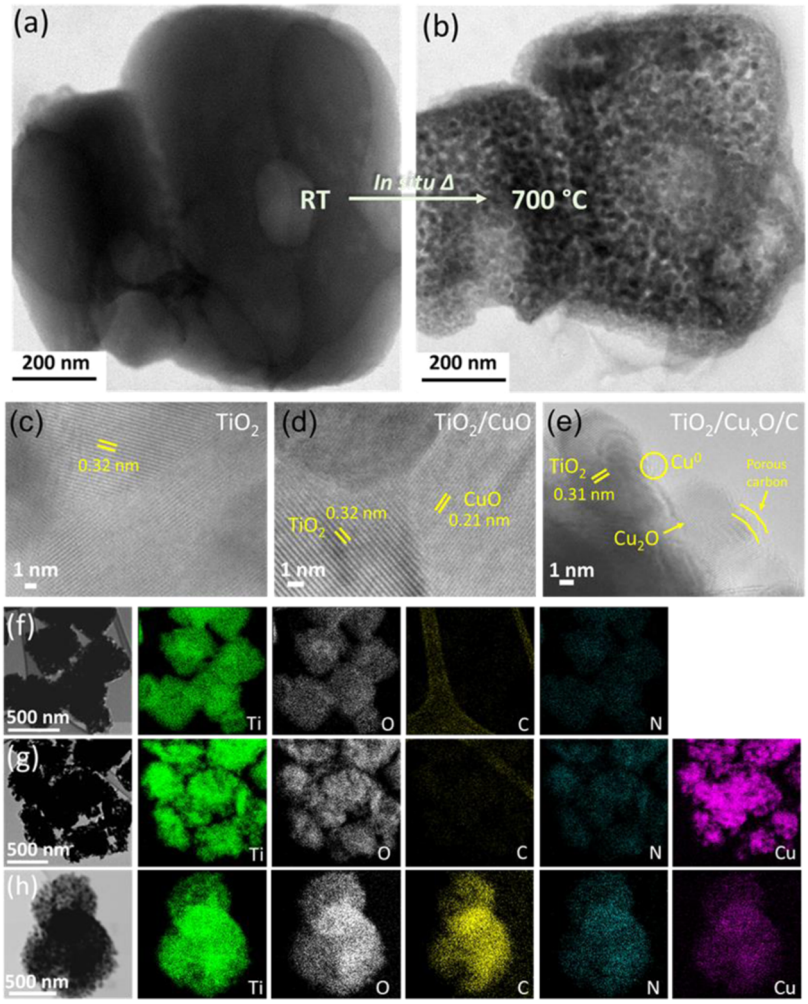

Figure 3. (a, b) In situ STEM images of selected particles of NH_2-MIL-125(Ti/Cu) obtained at RT and 700 °C under an Ar atmosphere. Representative high-resolution transmission electron microscopy (HRTEM) images of the derived samples (c) TiO_2, (d) TiO_2/CuO, and (e) TiO_2/Cu_xO/C. The EDX elemental maps of samples (f) TiO_2, (g) TiO_2/CuO, and (h) TiO_2/Cu_xO/C. The color codes representing the elements are as follows: green for Ti, gray for O, yellow for C, cyan for N, and magenta for Cu.

partially oxidizes, leaving a small amount of N-functionalized carbon (Figures 1c and 2e).

Morphology. As shown in Figure S8, scanning electron microscopy (SEM) images suggest that after pyrolyzing NH_2-MIL-125(Ti/Cu) at 700 °C, the disc-like morphology is retained in these derived composites. However, compared to the precursors, the particle surface turns rougher with cracks and cleavages. It is worth noting that in the sample TiO_2/CuO (Figure S8c) prepared by heat treatment of the precursor NH_2-MIL-125(Ti/Cu) at 700 °C under air, the surface is the roughest compared to other derived samples because a higher diffusion of Cu takes place at higher temperatures under air, and the absence of the carbon matrix causes a relatively higher mobilization of metal species, which consequently results in the deterioration of the disc-like morphology. However, under Ar/H_2O, the organic linker forms a porous carbon matrix; therefore, the formed carbon can immobilize the TiO_2 and Cu_xO nanoparticles, preserving the inherited morphology (Figure S8d).

In situ STEM images of NH_2-MIL-125(Ti/Cu) during the heating process from room temperature to 700 °C under inert conditions were recorded to monitor the morphology changes. The in situ STEM images (Figure 3a,b) show that during the heating of NH_2-MIL-125(Ti/Cu) under Ar up to 700 °C, the precursor NH_2-MIL-125(Ti/Cu) loses the periodicity of the isoreticular structure due to the cleaving off of coordination bonds between the organic linker and the Ti oxo-cluster. As confirmed by the TGA-MS results (Figure S4), the emission of gas species (CO_x, NH_x, and NO_x) initiates at above 350 °C, which causes the disintegration of the Ti oxo-cluster $[Ti_8O_8(OH)_4]$ and the organic linker $[O_2C-C_6H_3(NH_2)-CO_2]_6$, inevitably resulting in the shrinkage of particle sizes and the formation of micro-/mesoporous carbon from the organic linker, simultaneously recrystallizing the metal species into anatase/rutile TiO_2 and Cu_xO/Cu^0, as confirmed by XPS and PXRD. At 700 °C, the particles shrink approximately 35%, with an estimated width of 0.65 μm and the formation of mesopores in the carbon matrix (Figure 3b). In situ STEM clearly demonstrates the shrinkage of the particles, the formation of the mesoporous carbon matrix with uniformly immobilized TiO_2 and Cu_xO nanoparticles, and the preservation of the inherited morphology.[23]

High-resolution TEM images of derived TiO_2, TiO_2/CuO, and TiO_2/Cu_xO/C samples are shown in Figure 3c–e. The interfaces between particle boundaries of TiO_2, Cu_xO, and Cu^0 confirm that they are physically in contact to form

https://doi.org/10.1021/acs.energyfuels.2c02319
Energy Fuels XXXX, XXX, XXX−XXX

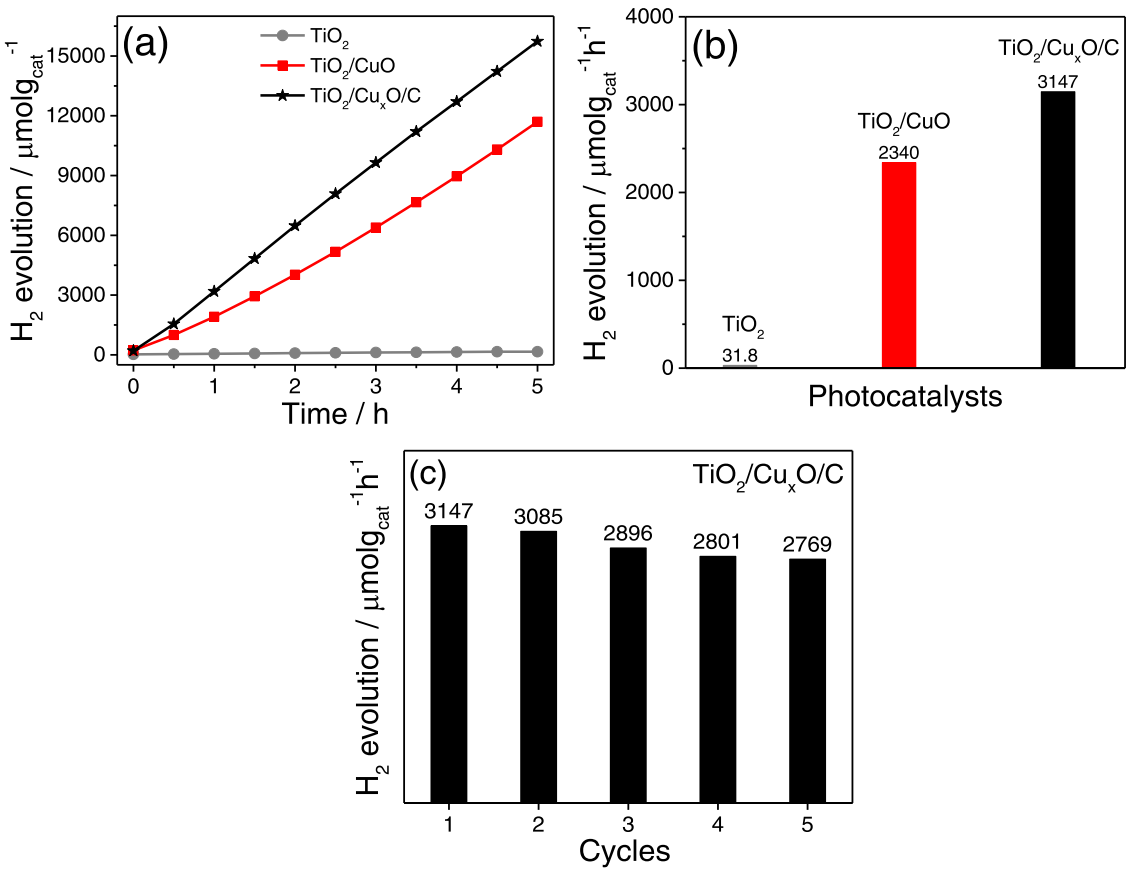

Figure 4. (a) Photocatalytic H_2 evolution. (b) Comparison of HER activities of derived composites TiO_2 (gray), TiO_2/CuO (red), and TiO_2/Cu_xO/C (black). (c) Recyclability study of the best-performing sample $TiO_2/Cu_xO/C_{2h}$.

heterojunctions. In samples derived under air (Figure 3d), anatase TiO_2 and CuO are the dominant crystalline phases (confirmed by PXRD) with measured interplanar spacings of 0.32 and 0.21 nm, respectively. However, in the sample TiO_2/Cu_xO/C (Figure 3e), anatase (101) and rutile (110) TiO_2 polymorphs as well as Cu_2O and Cu^0 nanoparticles can be clearly seen, embedded in the porous carbon matrix. Energy-dispersive X-ray (EDX) elemental mappings of the derived samples TiO_2, TiO_2/CuO, and TiO_2/Cu_xO/C (shown in Figure 3f–h) confirm that all of the elemental species (Ti, Cu, O, N, and C) are homogeneously distributed throughout the nanocomposite.[3,34,37] The p–n heterojunction formation between TiO_2 and Cu_xO, as well as the change in V.B. positions of the derived TiO_2, is further investigated by XPS and UV–vis absorption spectroscopy analyses.

Photocatalytic Hydrogen Evolution Performance. The photocatalytic HER performances of the derived TiO_2, TiO_2/CuO, and TiO_2/Cu_xO/C nanocomposites were evaluated in a methanol/water solution under UV–vis light (285 nm cutoff filter). No noble metals (Pt, Pd, or Au) were used as electron-mediating cocatalysts. The HER reactor setup is shown elsewhere.[24] As shown in Figure 4a,b, under UV–vis light, the HER performance of derived TiO_2, TiO_2/CuO, and TiO_2/Cu_xO/C nanocomposites increases with reaction time. After exposing to UV–vis light for 5 h, the derived TiO_2, TiO_2/CuO, and TiO_2/Cu_xO/C composites generated 159, 11 700, and 15 735 μmol g_{cat}^{-1} H_2, respectively. To systematically investigate the role of Cu_xO species and the porous carbon matrix in the photocatalytic HER activity, the H_2 evolution of the TiO_2/C composite (without loaded Cu) under identical experimental conditions was also tested. This TiO_2/C sample (carbon-containing) demonstrates an HER activity of 426 μmol g_{cat}^{-1} h^{-1}, 13 times higher compared to the bare TiO_2 (carbon-free). Moreover, the samples TiO_2/CuO (carbon-free) and TiO_2/Cu_xO/C (carbon-containing) exhibit HER activities of 2340 and 3147 μmol g_{cat}^{-1} h^{-1}, respectively, indicating the photocatalytic HER activity for the composite TiO_2/Cu_xO/C is 34% higher than that for the composite TiO_2/CuO. These observations clearly suggest that the presence of porous carbon in the composites offers media for charge migration and helps distribute the photocatalytic active sites on the porous carbon matrix without agglomerations. With more photocatalytic active sites being exposed, and the improved absorption of UV–vis light, TiO_2/Cu_xO/C results in improved HER performance of the composites. On the other hand, the sample TiO_2/CuO (Cu-containing) exhibits 2340 μmol g_{cat}^{-1} h^{-1} H_2 generation, 74 times higher than bare TiO_2 (Cu-free). Interestingly, the H_2 evolution of 3147 μmol g_{cat}^{-1} h^{-1} for the sample TiO_2/Cu_xO/C (Cu-containing) is 7.3 times for the sample TiO_2/C (Cu-free) under the same condition, which is also 99 times higher than that for the bare TiO_2. These observations clearly suggest that Cu species in the composites play a fundamental role in decreasing the EBGs by forming p–n heterojunctions between TiO_2 and Cu_xO species, increase the range of UV–vis light absorption, and consequently enhance the photocatalytic HER activity of TiO_2/Cu_xO/C composites.

Built on the observed photocatalytic HER performance and the physical as well as chemical characterizations of these different TiO_2-based composites obtained under similar

https://doi.org/10.1021/acs.energyfuels.2c02319
Energy Fuels XXXX, XXX, XXX–XXX

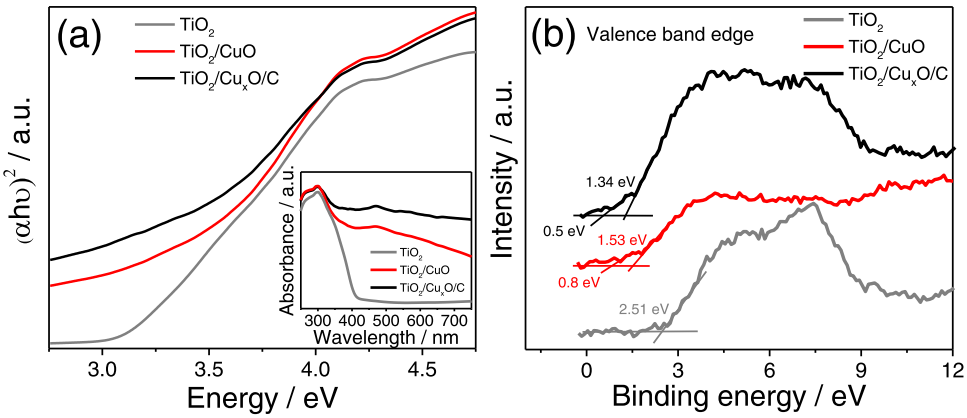

Figure 5. (a) Tauc plots (inset shows UV−vis absorption spectra) and (b) XPS valence band edge spectra of the derived samples TiO_2, TiO_2/CuO, and $TiO_2/Cu_xO/C$.

experimental conditions, it is clear that both porous carbon and Cu species are indispensable components in the $TiO_2/Cu_xO/C$ composite for photocatalytic application. However, the functionalized porous carbon matrix provides a platform for charge migration and offers a high surface area to better disperse the photocatalytic active sites. Additionally, codoped N and the Cu_xO species in $TiO_2/Cu_xO/C$ significantly contribute to enhancing the HER activity via the formation of multi-heterojunctions between TiO_2 and Cu_xO species.

To further elucidate the effect of the pyrolysis time on HER activity, two other samples derived from NH_2-MIL-125(Ti/Cu) with dwell times of 0.5 and 4 h, respectively, were tested under identical conditions. As shown in Figure S9, these samples ($TiO_2/Cu_xO/C_{0.5h}$ and $TiO_2/Cu_xO/C_{4h}$) exhibit HER activities of 1227 and 2338 μmol g_{cat}^{-1} h^{-1}, respectively, which are only 39 and 74% of the best sample $TiO_2/Cu_xO/C_{2h}$. This is due to the fact that the pyrolysis time of the precursor determines the crystallinity of the metal oxides and the textural properties of the porous carbon in the resulting composites, which consequently affects their photocatalytic HER performance. The apparent quantum yields (AQY %) of the derived samples are summarized in Table 1, and the detailed calculation of the AQY % for the selected sample is provided in the Supporting Information. Under the irradiation of visible light with a wavelength of 435 nm (in the range of EBGs of the photocatalysts), the apparent quantum yield of the most active nanocomposite $TiO_2/Cu_xO/C_{2h}$ is 7.66%, which is 38% higher than that of TiO_2/CuO and $TiO_2/Cu_xO/C_{4h}$. The recyclability of the best sample $TiO_2/Cu_xO/C_{2h}$ was also evaluated by running the photocatalytic HER test under identical conditions for 5 consecutive cycles. As shown in Figure 4c, this sample exhibits good recyclability and stability with a slight decrease of 12% in photocatalytic HER performance after 5 cycles, possibly due to the photocorrosion of the composite catalyst.[44] In these NH_2-MIL-125(Ti/Cu)-derived samples, TiO_2 and Cu_xO nanoparticles are distributed in the porous carbon matrix. Since Cu_xO is prone to photocorrosion in aqueous media under illumination, when the $TiO_2/Cu_xO/C$ catalyst is exposed to irradiated UV−vis light in an aqueous solution for a longer time, the photogenerated electrons will trigger self-reduction of Cu_xO species in an aqueous media, causing photocorrosion of the composite in a long-term recyclability test. Consequently, these partial electronic/structural changes in Cu_xO may gradually alter the nature of p−n heterostructures between TiO_2 and Cu_xO, which influences their EBG, as well as gradually change the decay or recombination of photogenerated charges. As a result, a slow decrease in photocatalytic efficiency is observed in the recyclability test.[44,45] Further experimental studies are required to investigate how to improve the chemical and physical stability of TiO_2 and Cu_xO against photocorrosion. Figure S10 presents a bar graph comparing the photocatalytic HER activities of some recently reported noble-metal-free, state-of-the-art TiO_2/CuO nanomaterials.[46−52] The $TiO_2/Cu_xO/C$ composite in our work is one of the best-performing composites for photocatalytic HER activity.

Mechanistic Insights into the Role of Different Components in $TiO_2/Cu_xO/C$ Composites for Photocatalytic HER Performance. UV−vis absorption spectra and XPS valence band edge (VBE) spectra were recorded to investigate the optical properties (Figure 5) of the derived composites. Estimated from the Tauc plots, the energy band gaps (EBGs) of the derived composites TiO_2, TiO_2/CuO, and $TiO_2/Cu_xO/C$ are 2.96, 2.64, and 2.45 eV, respectively. The narrowing of the EBGs in the MOF-derived samples compared to the pure TiO_2 (3.2 eV) can be attributed to the doped N and C species above the V.B. of TiO_2, the forming of the p−n heterojunction between TiO_2 and Cu_xO, and the presence of defects.[9,53] Additionally, in the sample $TiO_2/Cu_xO/C$, multi-heterostructures are formed due to the optimal ratio of anatase/rutile (A/R ratio of 1:1) TiO_2, as well as the presence of CuO and Cu_2O nanoparticles.[3,10] The UV−vis absorption spectra of the NH_2-MIL-125(Ti/Cu)-derived samples under Ar/H_2O at various pyrolysis times are shown in Figure S11a. The energy band gaps of samples $TiO_2/Cu_xO/C_{0.5h}$ and $TiO_2/Cu_xO/C_{4h}$ (from Tauc plots, Figure S11b) are estimated to be 2.33 and 2.38 eV, respectively. The relative shift in wavelength and peak intensity of the UV−vis absorption spectra and the subsequent change in energy band positions clearly indicate that the presence of the carbon matrix has a significant influence on the light absorption capabilities of these derived composites.

To investigate the shift in the energy band positions of the derived composites, high-resolution XPS spectra of the VBE were recorded. The VBE of the NH_2-MIL-125(Ti)-derived TiO_2 (Figure 5b) is observed at 2.51 eV, whereas the VBE spectra of the NH_2-MIL-125(Ti/Cu)-derived TiO_2/CuO under air show two shoulder-like bands at around 1.53 eV and 0.8 eV, respectively, assigned to the TiO_2 and CuO

https://doi.org/10.1021/acs.energyfuels.2c02319
Energy Fuels XXXX, XXX, XXX−XXX

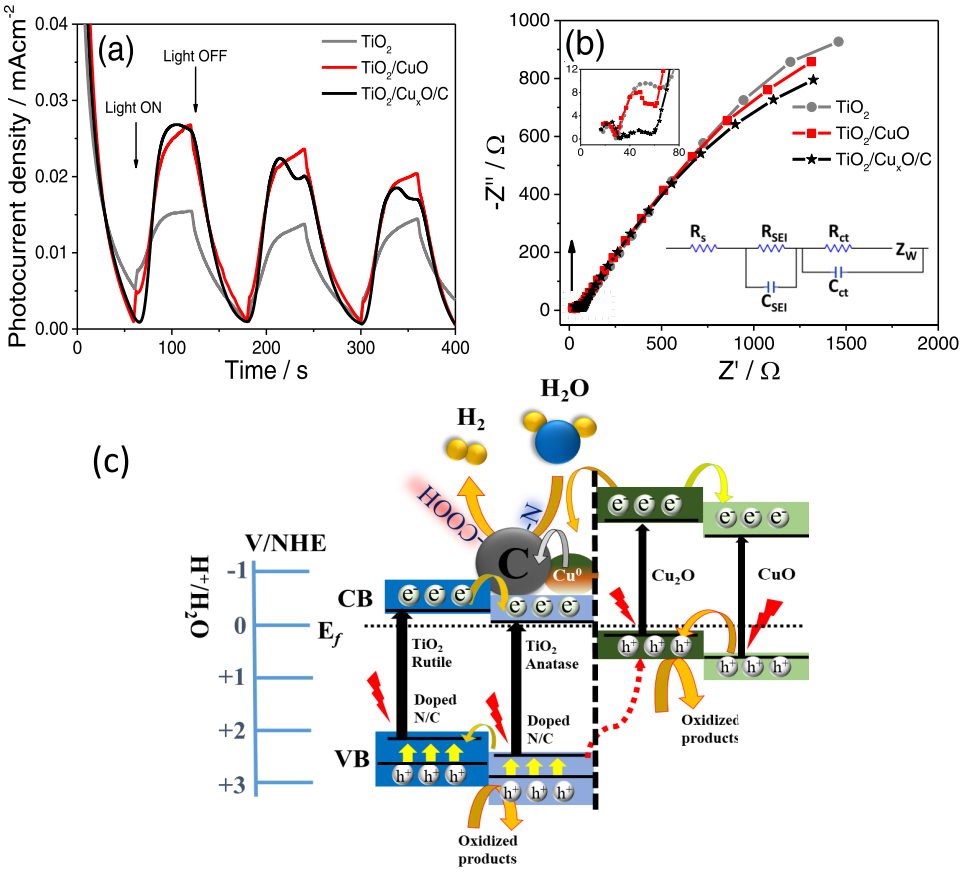

Figure 6. (a) Transient photocurrent density measured under simulated solar light with on-off cycles at the fixed potential (−0.4 V). (b) EIS Nyquist plots with the equivalent circuit diagram. (c) Schematic illustration of the energy band alignments and formation of multi-heterostructures for the $TiO_2/Cu_xO/C$ composite and the proposed mechanism of photocatalytic H_2 evolution.

nanoparticles.[24,54] In the sample $TiO_2/Cu_xO/C$, the VBEs of TiO_2 and Cu_xO shifted to 1.34 and 0.5 eV, respectively. A noticeable difference in the B.E. of Cu species from 0.8 to 0.5 eV in these samples also confirms that the Cu species are present predominantly in the Cu(I)/Cu(0) state in $TiO_2/Cu_xO/C$. A relatively bigger shift in the VBE of Ti species, from 2.51 eV for bare TiO_2 to 1.53 eV for TiO_2/CuO, can be attributed to the formation of a p−n heterojunction between TiO_2 and CuO, which causes band-bending at the interfaces (also confirmed by HRTEM).[24,34,37] A further shift in VBE of Ti toward lower B.E., 1.34 eV in the sample $TiO_2/Cu_xO/C$, is caused by the doped N and C species above the V.B. of TiO_2.[8,43] Supported by the PXRD patterns and the core-level XPS spectra, in the sample $TiO_2/Cu_xO/C$, the shift in VBE of TiO_2 and Cu_xO toward lower B.E. is attributed to the phasejunction formation between anatase and rutile TiO_2 with an optimized phase ratio of A/R ca. 1:1 and p−n heterojunction formation between TiO_2 and Cu_xO.[3,37,52,55]

The transient photocurrent density under an incident light and the subsequent charge transfer are the determining semiconducting properties of photocatalytic HER performance of a nanomaterial. The photocurrent densities (as a function of applied voltage) and the transportation of the photogenerated electrons on these MOF-derived materials were measured under simulated solar light. As shown in Figure 6a, samples TiO_2, TiO_2/CuO, and $TiO_2/Cu_xO/C$ exhibit photocurrent densities of 15, 26, and 27 $\mu A\ cm^{-2}$, respectively. An up to 2-fold increase in photocurrent density of the TiO_2/CuO composite compared to the bare TiO_2 clearly indicates that the p−n heterojunction formed between TiO_2 and CuO benefits the enhancement of the light absorption and the generation of photoelectrons. It is interesting to observe that the transient photocurrent density of the carbon-containing sample $TiO_2/Cu_xO/C$ is similar to the sample TiO_2/CuO. However, the shapes of their photocurrent density curves are different. Upon turning the light on, the transient photocurrent density in the sample $TiO_2/CuO/C$ instantly reaches the maximum value and remains relatively stable until the incident light is switched off. However, the TiO_2/CuO composite (and also TiO_2) shows a gradual increase in the photocurrent density before reaching the maximum value. Comparing the intensities and shapes of the curves for transient photocurrent densities of these samples, it is likely that the photogeneration of electrons and holes primarily takes place on metal oxides, but the charge recombination and charge transport depend on the available charge migration pathways within the sample.[6,56] The instantaneous increase in photocurrent density up to the maximum value in the composite $TiO_2/Cu_xO/C$ upon light exposure indicates that the presence of porous carbon improves the electrical conductivity and provides additional charge migration pathways and, consequently, slows down the decay/recombination of photogenerated charges. In addition, the functionalized hydrophilic porous carbon matrix also provides enhanced interaction between adsorbed water molecules and the photogenerated electrons.[22,24]

Electrochemical impedance spectroscopy (EIS) was performed to determine the electric charge-transfer resistance (R_{ct}) of these derived nanocomposites. As shown in Figure 6b,

https://doi.org/10.1021/acs.energyfuels.2c02319
Energy Fuels XXXX, XXX, XXX−XXX

two semicircles were observed, which can be assigned to the formation of a passivation layer at the solid electrolyte interface (R_{SEI}), the charge-transfer resistance (R_{ct}) as well as the Warbung element (Z_W) in the low-frequency region. The R_{ct} value can be estimated from the diameter of the arc/semicircle in the high-frequency region of the Nyquist plots. The R_{ct} values of TiO_2, TiO_2/CuO, and TiO_2/Cu_xO/C are estimated to be 40, 33, and 25 Ω, respectively. A decrease in the R_{ct} values of TiO_2/CuO and TiO_2/Cu_xO/C compared to the bare TiO_2 confirms that the in situ-formed multi-heterojunctions (anatase-rutile phasejunction and TiO_2−Cu_xO p−n heterojunction) offer multiple pathways for charge migration, resulting in the improvement of the charge-transfer efficiencies of the derived composites. It is worth highlighting that the R_{ct} value of the carbon-containing sample TiO_2/Cu_xO/C is smaller compared to TiO_2/CuO, which clearly indicates that the porous carbon matrix in these derived composites contributes to the electrical conductivity by minimizing the charge-transfer resistance. The measured photocurrent responses and R_{ct} values of these composites are well consistent with their photocatalytic HER performances. To further investigate the charge generation mechanism in these composites, electron paramagnetic resonance (EPR) spectrum of a representative sample TiO_2/Cu_xO/C was measured under UV−vis light for 10 min at 77 K in vacuum conditions. Figure S12 shows that a sharp signal appears at the g factor of 1.97, which represents the presence of Ti^{3+}. Another high-intensity signal observed at the g factor of 2.002 (closer to the g factor for the free electrons, 2.0023) is due to the formation of carbon-centered radicals ($C^{\bullet}$). In pure TiO_2, this signal is not observed.[57] The formation of $C^{\bullet}$ upon irradiation of UV−vis light suggests that the underlying paramagnetic species might be related to the photocatalytic reaction in the carbon-doped TiO_2.[57,58]

Based on the various characterizations and in-depth analysis, the photocatalytic mechanism (as proposed in Figure 6c) and the origin of photocatalytic H_2 evolution activities in the bi-MOF-derived nanocomposites can be elucidated. The best-performing sample, TiO_2/Cu_xO/C, consists of the TiO_2 polymorph and Cu_xO/CuO and Cu^0 species, uniformly distributed in the porous carbon matrix. Due to the optimal ratio (A/R 1:0.96, close to 1:1) and the staggered (type-II) valence/conduction band positions, the TiO_2 polymorph forms a phasejunction between A (101) and R (110) phases.[10] Photogenerated electrons in the conduction band (C.B.) preferably migrate from the rutile to the anatase phase of TiO_2 due to its higher electron affinity.[55] Simultaneously, the photogenerated holes (h^+) in V.B. can migrate to the opposite direction, from anatase to the rutile phase of TiO_2. In TiO_2/Cu_xO/C, in situ-doped N and C species elevate the VBEs of anatase and rutile TiO_2 closer to the Fermi level by forming additional carbon- and oxygen-rich intraband/interstitial (N−O-like) electronic states. This further narrows down the overall energy band gap of TiO_2 to 2.45 eV compared to that of the pure TiO_2 (3.2 eV) and consequently enhances the visible-light absorption and charge generation.[22,43]

The second significant factor in photocatalytic HER activity of these nanocomposites is the formation of the heterostructure between Cu_2O and CuO nanoparticles. Confirmed by the PXRD patterns and high-resolution XPS spectra, the VBEs of Cu_2O and CuO lie at 932.9 and 934.9 eV (core levels), respectively, which can form the heterojunction between Cu_2O and CuO nanoparticles.[24,34,59] More importantly, the VBE estimated from the XPS of the Cu_2O/CuO species lies at around 0.8 eV below the Fermi level. Such an energy band alignment between the C.B. of TiO_2 and the V.B. of Cu_xO nanoparticles (respecting the Fermi level) favors the p−n heterojunction formation between the highly crystalline TiO_2 polymorph and Cu_xO particles. Moreover, the Cu^0 nanoparticles (evidenced by PXRD) present in this sample can further promote a faster photogenerated electron transfer from the C.B. of Cu_2O to CuO, the anatase TiO_2 nanoparticle, or the porous carbon. The availability of multiple charge-transfer pathways can significantly suppress the possibilities of charge recombination. The presence of a functionalized carbon matrix (with −N and −OH/−COOH groups) keeps the metal oxide species homogeneously distributed, preventing bulk agglomeration. Such spatial distribution of the metal compounds ensures the maximum exposure of the photocatalytic active sites and the reactant species, hence improving the efficiency of the photocatalytic HER performance. On the other hand, it is obvious that no heterostructure is formed in NH_2-MIL-125(Ti)-derived TiO_2 under air. However, in NH_2-MIL-125(Ti/Cu)-derived TiO_2/CuO under air, the photocatalytic activity largely originates from the p−n heterojunction formed between the highly crystalline TiO_2 polymorph and CuO nanoparticles. In other NH_2-MIL-125(Ti/Cu)-derived samples, the poorly crystalline metal oxide species in the sample TiO_2/Cu_xO/$C_{0.5h}$, the absence of the optimized ratios of the TiO_2 polymorph and dominant CuO species, and the negligible amount of carbon in the sample TiO_2/Cu_xO/C_{4h} are the primary reasons behind their relatively poor HER performance. It can be inferred that electron-rich anatase TiO_2 and CuO nanoparticles act as photocatalytic active sites where the photocatalytic reaction takes place to reduce H_2O into H_2, while the V.B.s of rutile TiO_2 and Cu_2O nanoparticles act as hole-scavenging platforms to complete the other half-reaction.

This work is an attempt to elucidate the origin of photocatalytic HER activities of NH_2-MIL-125(Ti/Cu)-derived TiO_2/Cu_xO/C nanocomposites by systematic investigation of the contribution of each component, including TiO_2, Cu_xO, and porous carbon species in composites. Employing the bi-MOF as a precursor, in situ tunable multi-heterostructures uniformly distributed in a selectively functionalized carbon matrix can be readily produced via a simple one-step method under appropriate pyrolysis conditions. This method offers a simple route to in situ tune the compositions, structures, morphologies, and the semiconducting properties of the derived composites to achieve high HER performance photocatalysts without noble metals.

CONCLUSIONS

The TiO_2/Cu_xO/C nanocomposite derived from NH_2-MIL-125(Ti/Cu) under Ar/H_2O at 700 °C for 2 h exhibited highest photocatalytic H_2 evolution activity. Supported by various characterizations and in-depth analysis, high photocatalytic activity is due to the formation of phasejunctions between well-crystallized anatase/rutile TiO_2 polymorph with an optimized ratio, N/C codoping, p−n heterojunction between the TiO_2 and Cu_xO nanoparticles, and their uniform distribution in a functionalized porous carbon matrix. These nanocomposites enable increased visible-light absorption due to the relatively narrower energy band gaps and the improved spatial separation of photogenerated charges resulting from the simultaneous formation of type-II staggered phasejunction and p−n

https://doi.org/10.1021/acs.energyfuels.2c02319
Energy Fuels XXXX, XXX, XXX−XXX

heterojunction. The optimized nanocomposites with in situ-formed multi-heterostructures offer multiple pathways of charge migration, resulting in lower charge-transfer resistance and suppressed bulk charge recombination. Therefore, such metal oxide multi-heterojunctions homogeneously dispersed in the functionalized porous carbon matrix provide easily accessible active sites for enhanced photocatalytic HER activity without expensive noble metal cocatalysts.

■ ASSOCIATED CONTENT

Supporting Information

The Supporting Information is available free of charge at https://pubs.acs.org/doi/10.1021/acs.energyfuels.2c02319.

XRD, gas sorption, textural properties, TEM, XPS depth profile and TGA data of precursors as well as XRD, gas sorption, TGA, SEM, UV−vis spectra, EPR, and photocatalytic HER data of different $TiO_2/Cu_xO/C$ samples (PDF)

■ AUTHOR INFORMATION

Corresponding Authors

Mian Zahid Hussain − *College of Engineering, Mathematics and Physical Sciences, University of Exeter, Exeter EX4 4QF, U.K.; School of Natural Sciences and Catalysis Research Center, Technical University of Munich (TUM), 85748 Garching, Germany*; Email: ge68muq@tum.de

Yongde Xia − *College of Engineering, Mathematics and Physical Sciences, University of Exeter, Exeter EX4 4QF, U.K.*; orcid.org/0000-0001-9686-8688; Email: Y.Xia@exeter.ac.uk

Authors

Zhuxian Yang − *College of Engineering, Mathematics and Physical Sciences, University of Exeter, Exeter EX4 4QF, U.K.*

Bart van der Linden − *Catalysis Engineering, Chemical Engineering Department, Delft University of Technology, 2629 HZ Delft, Netherlands*; orcid.org/0000-0003-1384-7457

Werner R. Heinz − *School of Natural Sciences and Catalysis Research Center, Technical University of Munich (TUM), 85748 Garching, Germany*

Mounib Bahri − *Institut de Physique et Chimie des Matériaux de Strasbourg (IPCMS), UMR 7504 CNRS, Université de Strasbourg, 67034 Strasbourg, France*

Ovidiu Ersen − *Institut de Physique et Chimie des Matériaux de Strasbourg (IPCMS), UMR 7504 CNRS, Université de Strasbourg, 67034 Strasbourg, France*; orcid.org/0000-0002-1553-0915

Quanli Jia − *Henan Key Laboratory of High Temperature Functional Ceramics, Zhengzhou University, Zhengzhou 450052, China*

Roland A. Fischer − *School of Natural Sciences and Catalysis Research Center, Technical University of Munich (TUM), 85748 Garching, Germany*; orcid.org/0000-0002-7532-5286

Yanqiu Zhu − *College of Engineering, Mathematics and Physical Sciences, University of Exeter, Exeter EX4 4QF, U.K.*; orcid.org/0000-0003-3659-5643

Complete contact information is available at: https://pubs.acs.org/10.1021/acs.energyfuels.2c02319

Author Contributions

M.Z.H.: Investigation, methodology, data curation, writing—original draft. Z.Y.: Data curation, validation, writing—review & editing. B.v.d.L.: Methodology, data curation, validation. W.R.H.: Investigation, validation, data curation. M.B.: Investigation, validation, data curation. O.E.: Methodology, writing—review & editing. Q.J.: Investigation, data curation. R.A.F.: Supervision, writing—review & editing. Y.Z.: Supervision, writing—review & editing. Y.X.: Supervision, conceptualization, methodology, validation, writing—review & editing.

Notes

The authors declare no competing financial interest.

■ ACKNOWLEDGMENTS

The authors are thankful to TUM Innovation Network Artificial Intelligence in Material Science (ARTEMIS), EPSRC CDT in Metamaterials at the University of Exeter, Leverhulme Trust (RPG-2018-320), and Royal Society (IEC \NSFC\201121) for financial support.

■ REFERENCES

(1) Fayomi, G. U.; Mini, S. E.; Fayomi, O. S. I.; Oyeleke, O.; Omole, D. O.; Akinwumi, I. I. Overview of Industrial Pollution Activities and its Curbing Mechanisms. *IOP Conf. Ser.: Mater. Sci. Eng.* **2019**, *640*, No. 012097.

(2) Cao, S.; Piao, L.; Chen, X. Emerging Photocatalysts for Hydrogen Evolution. *Trends Chem.* **2020**, *2*, 57−70.

(3) Low, J.; Yu, J.; Jaroniec, M.; Wageh, S.; Al-Ghamdi, A. A. Heterojunction Photocatalysts. *Adv. Mater.* **2017**, *29*, No. 1601694.

(4) Barelli, L.; Bidini, G.; Gallorini, F.; Servili, S. Hydrogen Production through Sorption-Enhanced Steam Methane Reforming and Membrane Technology: A Review. *Energy* **2008**, *33*, 554−570.

(5) Fujishima, A.; Honda, K. Electrochemical Photolysis of Water at a Semiconductor Electrode. *Nature* **1972**, *238*, 37−38.

(6) Kumar, S. G.; Devi, L. G. Review on Modified TiO_2 Photocatalysis under UV/Visible Light: Selected Results and Related Mechanisms on Interfacial Charge Carrier Transfer Dynamics. *J. Phys. Chem. A* **2011**, *115*, 13211−13241.

(7) Rahimi, N.; Pax, R. A.; Gray, E. M. Review of Functional Titanium Oxides. I: TiO_2 and its Modifications. *Prog. Solid State Chem.* **2016**, *44*, 86−105.

(8) Asahi, R.; Morikawa, T.; Ohwaki, T.; Aoki, K.; Taga, Y. Visible-Light Photocatalysis in Nitrogen-Doped Titanium Oxides. *Science* **2001**, *293*, 269.

(9) Schneider, J.; Matsuoka, M.; Takeuchi, M.; Zhang, J.; Horiuchi, Y.; Anpo, M.; Bahnemann, D. W. Understanding TiO_2 Photocatalysis: Mechanisms and Materials. *Chem. Rev.* **2014**, *114*, 9919−9986.

(10) Su, R.; Bechstein, R.; Sø, L.; Vang, R. T.; Sillassen, M.; Esbjörnsson, B.; Palmqvist, A.; Besenbacher, F. How the Anatase-to-Rutile Ratio Influences the Photoreactivity of TiO_2. *J. Phys. Chem. C* **2011**, *115*, 24287−24292.

(11) Fu, J.; Yu, J.; Jiang, C.; Cheng, B. g-C_3N_4-Based Heterostructured Photocatalysts. *Adv. Energy Mater.* **2018**, *8*, No. 1701503.

(12) Takanabe, K. Photocatalytic Water Splitting: Quantitative Approaches toward Photocatalyst by Design. *ACS Catal.* **2017**, *7*, 8006−8022.

(13) Zhou, H.-C.; L, J. R.; Yaghi, O. M. Introduction to Metal−Organic Frameworks. *Chem. Rev.* **2012**, *112*, 673−674.

(14) Li, H.; Eddaoudi, M.; O'Keeffe, M.; Yaghi, O. M. Design and Synthesis of An Exceptionally Stable and Highly Porous Metal-Organic Framework. *Nature* **1999**, *402*, 276−279.

(15) Nasalevich, M. A.; van der Veen, M.; Kapteijn, F.; Gascon, J. Metal−Organic Frameworks as Heterogeneous Photocatalysts: Advantages and Challenges. *CrystEngComm* **2014**, *16*, 4919−4926.

(16) Luo, H.; Zeng, Z.; Zeng, G.; Zhang, C.; Xiao, R.; Huang, D.; Lai, C.; Cheng, M.; Wang, W.; Xiong, W.; et al. Recent Progress on Metal-organic Frameworks Based- and Derived-Photocatalysts for Water Splitting. *Chem. Eng. J.* **2020**, *383*, No. 123196.
(17) Das, R.; Pachfule, P.; Banerjee, R.; Poddar, P. Metal and Metal Oxide Nanoparticle Synthesis from Metal Organic Frameworks (MOFs): Finding the Border of Metal and Metal Oxides. *Nanoscale* **2012**, *4*, 591−599.
(18) Song, F.; Li, W.; Sun, Y. Metal−Organic Frameworks and Their Derivatives for Photocatalytic Water Splitting. *Inorganics* **2017**, *5*, 40.
(19) Zeng, L.; Guo, X.; He, C.; Duan, C. Metal−Organic Frameworks: Versatile Materials for Heterogeneous Photocatalysis. *ACS Catal.* **2016**, *6*, 7935−7947.
(20) Hussain, M. Z.; Yang, Z.; Huang, Z.; Jia, Q.; Zhu, Y.; Xia, Y. Recent Advances in Metal−Organic Frameworks Derived Nanocomposites for Photocatalytic Applications in Energy and Environment. *Adv. Sci.* **2021**, *8*, No. 2100625.
(21) Hussain, M. Z.; Yang, Z.; Khalil, A. M. E.; Hussain, S.; Awan, S. U.; Jia, Q.; Fischer, R. A.; Zhu, Y.; Xia, Y. Metal-organic Framework Derived Multi-functionalized and Co-doped TiO_2/C Nanocomposites for Excellent Visible-light Photocatalysis. *J. Mater. Sci. Technol.* **2022**, *101*, 49−59.
(22) Hussain, M. Z.; Yang, Z.; van der Linden, B.; Huang, Z.; Jia, Q.; Cerrato, E.; Fischer, R. A.; Kapteijn, F.; Zhu, Y.; Xia, Y. Surface Functionalized N-C-TiO_2/C Nanocomposites Derived from Metal-organic Framework in Water Vapour for Enhanced Photocatalytic H_2 Generation. *J. Energy Chem.* **2021**, *57*, 485−495.
(23) Hussain, M. Z.; Bahri, M.; Heinz, W. R.; Jia, Q.; Ersen, O.; Kratky, T.; Fischer, R. A.; Zhu, Y.; Xia, Y. An In Situ Investigation of the Thermal Decomposition of Metal-organic Framework NH_2-MIL-125 (Ti). *Microporous Mesoporous Mater.* **2021**, *316*, No. 110957.
(24) Hussain, M. Z.; van der Linden, B.; Yang, Z.; Jia, Q.; Chang, H.; Fischer, R. A.; Kapteijn, F.; Zhu, Y.; Xia, Y. Bimetal−organic Framework Derived Multi-heterostructured TiO_2/Cu_xO/C Nanocomposites with Superior Photocatalytic H_2 Generation Performance. *J. Mater. Chem. A* **2021**, *9*, 4103−4116.
(25) Huang, Z.; Yang, Z.; Jia, Q.; Wang, N.; Zhu, Y.; Xia, Y. Bimetallic Co-Mo Sulfide/carbon Composites Derived from Polyoxometalate Encapsulated Polydopamine-decorated ZIF Nanocubes for Efficient Hydrogen and Oxygen Evolution. *Nanoscale* **2022**, *14*, 4726−4739.
(26) Huang, Z.; Yang, Z.; Hussain, M. Z.; Jia, Q.; Zhu, Y.; Xia, Y. Bimetallic Fe-Mo Sulfide/carbon Nanocomposites Derived from Phosphomolybdic Acid Encapsulated MOF for Efficient Hydrogen Generation. *J. Mater. Sci. Technol.* **2021**, *84*, 76−85.
(27) Yuan, L.; Han, C.; Yang, M.-Q.; Xu, Y.-J. Photocatalytic Water Splitting for Solar Hydrogen Generation: Fundamentals and Recent Advancements. *Int. Rev. Phys. Chem.* **2016**, *35*, 1−36.
(28) Oar-Arteta, L.; Wezendonk, T.; Sun, X.; Kapteijn, F.; Gascon, J. Metal Organic Frameworks as Precursors for the Manufacture of Advanced Catalytic Materials. *Mater. Chem. Front.* **2017**, *1*, 1709−1745.
(29) Xia, W.; Mahmood, A.; Zou, R.; Xu, Q. Metal−organic Frameworks and Their Derived Nanostructures for Electrochemical Energy Storage and Conversion. *Energy Environ. Sci.* **2015**, *8*, 1837−1866.
(30) Ferrari, A. C.; Robertson, J. Interpretation of Raman Spectra of Disordered and Amorphous Carbon. *Phys. Rev. B* **2000**, *61*, 14095−14107.
(31) Bokobza, L.; Bruneel, J.-L.; Couzi, M. Raman Spectra of Carbon-Based Materials (from Graphite to Carbon Black) and of Some Silicone Composites. *C* **2015**, *1*, 77−94.
(32) Hussain, M. Z.; Pawar, G. S.; Huang, Z.; Tahir, A. A.; Fischer, R. A.; Zhu, Y.; Xia, Y. Porous ZnO/Carbon Nanocomposites Derived from Metal Organic Frameworks for Highly Efficient Photocatalytic Applications: A Correlational Study. *Carbon* **2019**, *146*, 348−363.
(33) Huang, Z.; Yang, Z.; Hussain, M. Z.; Chen, B.; Jia, Q.; Zhu, Y.; Xia, Y. Polyoxometallates@zeolitic-imidazolate-framework Derived Bimetallic Tungsten-cobalt Sulfide/Porous Carbon Nanocomposites as Efficient Bifunctional Electrocatalysts for Hydrogen and Oxygen Evolution. *Electrochim. Acta* **2020**, *330*, No. 135335.
(34) Shi, Q.; Ping, G.; Wang, X.; Xu, H.; Li, J.; Cui, J.; Abroshan, H.; Ding, H.; Li, G. CuO/TiO_2 Heterojunction Composites: An Efficient Photocatalyst for Selective Oxidation of Methanol to Methyl Formate. *J. Mater. Chem. A* **2019**, *7*, 2253−2260.
(35) Chen, X.; Burda, C. The Electronic Origin of the Visible-Light Absorption Properties of C-, N- and S-Doped TiO_2 Nanomaterials. *J. Am. Chem. Soc.* **2008**, *130*, 5018−5019.
(36) Hussain, M. Z.; Schneemann, A.; Fischer, R. A.; Zhu, Y.; Xia, Y. MOF Derived Porous ZnO/C Nanocomposites for Efficient Dye Photodegradation. *ACS Appl. Energy Mater.* **2018**, *1*, 4695−4707.
(37) Zhang, Y.; Hu, W.; Wang, D.; Reinhart, B. J.; Huang, J. Electron Shuttle in the MOF Derived TiO_2/CuO Heterojunction Boosts Light Driven Hydrogen Evolution. *J. Mater. Chem. A* **2021**, *9*, 6180−6187.
(38) Yano, T.; Ebizuka, M.; Shibata, S.; Yamane, M. Anomalous Chemical Shifts of Cu_{2p} and Cu_{LMM} Auger Spectra of Silicate Glasses. *J. Electron Spectrosc. Relat. Phenom.* **2003**, *131-132*, 133−144.
(39) Hiraba, H.; Koizumi, H.; Kodaira, A.; Takehana, K.; Yoneyama, T.; Matsumura, H. Effects of Copper Surface Oxidation and Reduction on Shear-Bond Strength Using Functional Monomers. *Materials* **2021**, *14*, 1753.
(40) Pels, J. R.; Kapteijn, F.; Moulijn, J. A.; Zhu, Q.; Thomas, K. M. Evolution of Nitrogen Functionalities in Carbonaceous Materials during Pyrolysis. *Carbon* **1995**, *33*, 1641−1653.
(41) Bhadra, B. N.; Vinu, A.; Serre, C.; Jhung, S. H. MOF-derived Carbonaceous Materials Enriched with Nitrogen: Preparation and Applications in Adsorption and Catalysis. *Mater. Today* **2019**, *25*, 88−111.
(42) Amreetha, S.; Dhanuskodi, S.; Nithya, A.; Jothivenkatachalam, K. Three Way Electron Transfer of a C−N−S Tri doped Two-phase Junction of TiO_2 Nanoparticles for Efficient Visible Light Photocatalytic Dye Degradation. *RSC Adv.* **2016**, *6*, 7854−7863.
(43) Di Valentin, C.; Finazzi, E.; Pacchioni, G.; Selloni, A.; Livraghi, S.; Paganini, M. C.; Giamello, E. N-doped TiO_2: Theory and Experiment. *Chem. Phys.* **2007**, *339*, 44−56.
(44) Xing, H.; E, L.; Guo, Z.; Zhao, D.; Li, X.; Liu, Z. Exposing the Photocorrosion Mechanism and Control Strategies of a CuO Photocathode. *Inorg. Chem. Front.* **2019**, *6*, 2488−2499.
(45) Wang, K.; Bielan, Z.; Endo-Kimura, M.; Janczarek, M.; Zhang, D.; Kowalski, D.; Zielińska-Jurek, A.; Markowska-Szczupak, A.; Ohtani, B.; Kowalska, E. On the Mechanism of Photocatalytic Reactions on Cu_xO@TiO_2 Core−shell Photocatalysts. *J. Mater. Chem. A* **2021**, *9*, 10135−10145.
(46) Karthik, P.; Shaheer, A. R. M.; Vinu, A.; Neppolian, B. Amine Functionalized Metal−Organic Framework Coordinated with Transition Metal Ions: d−d Transition Enhanced Optical Absorption and Role of Transition Metal Sites on Solar Light Driven H_2 Production. *Small* **2020**, *16*, No. 1902990.
(47) Kampouri, S.; Ireland, C. P.; Valizadeh, B.; Oveisi, E.; Schouwink, P. A.; Mensi, M.; Stylianou, K. C. Mixed-Phase MOF-Derived Titanium Dioxide for Photocatalytic Hydrogen Evolution: The Impact of the Templated Morphology. *ACS Appl. Energy Mater.* **2018**, *1*, 6541−6548.
(48) Hou, H.; Shang, M.; Gao, F.; Wang, L.; Liu, Q.; Zheng, J.; Yang, Z.; Yang, W. Highly Efficient Photocatalytic Hydrogen Evolution in Ternary Hybrid TiO_2/CuO/Cu Thoroughly Mesoporous Nanofibers. *ACS Appl. Mater. Interfaces* **2016**, *8*, 20128−20137.
(49) Xiang, Q.; Yu, J.; Jaroniec, M. Enhanced photocatalytic H_2-production Activity of Graphene-modified Titania Nanosheets. *Nanoscale* **2011**, *3*, 3670−3678.
(50) Zhang, Y.-H.; Li, Y.-L.; Jiu, B.-B.; Gong, F.-L.; Chen, J.-L.; Fang, S.-M.; Zhang, H.-L. Highly Enhanced Photocatalytic H_2 Evolution of Cu_2O Microcube by Coupling with TiO_2 Nanoparticles. *Nanotechnology* **2019**, *30*, No. 145401.
(51) Li, R.; Wu, S.; Wan, X.; Xu, H.; Xiong, Y. Cu/TiO_2 Octahedral-shell Photocatalysts Derived from Metal−organic Framework@ semiconductor Hybrid Structures. *Inorg. Chem. Front.* **2016**, *3*, 104−110.

https://doi.org/10.1021/acs.energyfuels.2c02319
Energy Fuels XXXX, XXX, XXX−XXX

(52) Liao, Y.-T.; Huang, Y.-Y.; Chen, H. M.; Komaguchi, K.; Hou, C.-H.; Henzie, J.; Yamauchi, Y.; Ide, Y.; Wu, K. C. W. Mesoporous TiO_2 Embedded with a Uniform Distribution of CuO Exhibit Enhanced Charge Separation and Photocatalytic Efficiency. *ACS Appl. Mater. Interfaces* **2017**, *9*, 42425−42429.
(53) Kubacka, A.; Fernández-García, M.; Colón, G. Advanced Nanoarchitectures for Solar Photocatalytic Applications. *Chem. Rev.* **2012**, *112*, 1555−1614.
(54) Serpone, N.; Emeline, A. V.; Ryabchuk, V. K.; Kuznetsov, V. N.; Artem'ev, Y. M.; Horikoshi, S. Why do Hydrogen and Oxygen Yields from Semiconductor-Based Photocatalyzed Water Splitting Remain Disappointingly Low? Intrinsic and Extrinsic Factors Impacting Surface Redox Reactions. *ACS Energy Lett.* **2016**, *1*, 931−948.
(55) Scanlon, D. O.; Dunnill, C. W.; Buckeridge, J.; Shevlin, S. A.; Logsdail, A. J.; Woodley, S. M.; Catlow, C. R. A.; Powell, M. J.; Palgrave, R. G.; Parkin, I. P.; et al. Band Alignment of Rutile and Anatase TiO_2. *Nat. Mater.* **2013**, *12*, 798−801.
(56) Peter, L. M.; Wijayantha, K. G. U.; Tahir, A. A. Kinetics of Light-driven Oxygen Evolution at α-Fe_2O_3 Electrodes. *Faraday Discuss.* **2012**, *155*, 309−322.
(57) Qiu, B.; Zhou, Y.; Ma, Y.; Yang, X.; Sheng, W.; Xing, M.; Zhang, J. Facile Synthesis of the Ti^{3+} Self-doped TiO_2-graphene Nanosheet Composites with Enhanced Photocatalysis. *Sci. Rep.* **2015**, *5*, No. 8591.
(58) Chiesa, M.; Paganini, M. C.; Livraghi, S.; Giamello, E. Charge trapping in TiO_2 polymorphs as seen by Electron Paramagnetic Resonance spectroscopy. *Phys. Chem. Chem. Phys.* **2013**, *15*, 9435−9447.
(59) Zhen, W.; Jiao, W.; Wu, Y.; Jing, H.; Lu, G. The Role of a Metallic Copper Interlayer during Visible Photocatalytic Hydrogen Generation over a $Cu/Cu_2O/Cu/TiO_2$ Catalyst. *Catal. Sci. Technol.* **2017**, *7*, 5028−5037.

https://doi.org/10.1021/acs.energyfuels.2c02319
Energy Fuels XXXX, XXX, XXX−XXX